Journal of
Materials Chemistry C

Materials for optical, magnetic and electronic devices

Accepted Manuscript

This article can be cited before page numbers have been issued, to do this please use: D. Mara, L. Pilia, M. Van De Steen, I. Miletto, M. Zeng, K. Van Hecke, A. Serpe, P. Deplano, R. Van Deun and F. Artizzu, *J. Mater. Chem. C*, 2021, DOI: 10.1039/D1TC04191F.

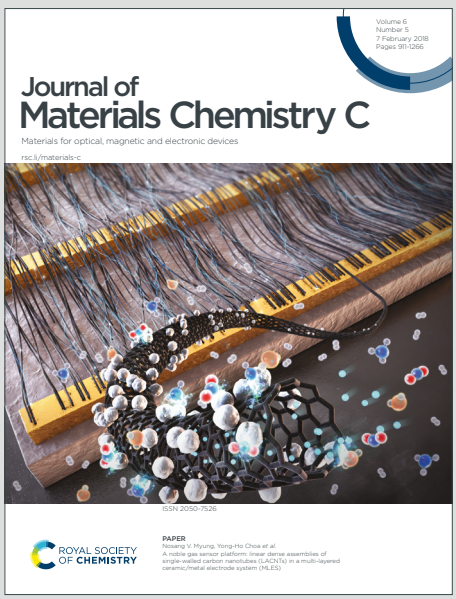

ROYAL SOCIETY OF CHEMISTRY

rsc.li/materials-c

View Article Online
DOI: 10.1039/D1TC04191F

ARTICLE

Single-component panchromatic white light generation, tuneable excimer-like visible orange and NIR emission in a Dy quinolinolate complex

Received 00th January 20xx,
Accepted 00th January 20xx

DOI: 10.1039/x0xx00000x

Dimitrije Mara,[a] Luca Pilia,[b] Maxim Van de Steen,[c] Ivana Miletto,[d] Min Zeng,[e] Kristof Van Hecke,[c] Angela Serpe,[f] Paola Deplano,[f] Rik Van Deun[c] and Flavia Artizzu[c,d,*]

Panchromatic single-component pure white light generation with a PLQY of ~14.5% is obtained from a dysprosium complex with the 5,7-dichloro-8-quinolinol ligand (HClQ) thanks to a peculiar orange-red excimer-like emission induced by π-staking interactions between discrete dimeric units in the crystal packing. The emission color is highly tunable by phase change and mechanical stimuli. Remarkably, this compound also displays Dy-centered NIR emission at telecommunication wavelengths upon photoexcitation over an extraordinarily broad spectral range.

Introduction

Colour-tuneable white light luminescent molecular materials attract great interest for a wide range of applications such as flat panel displays, illumination, sensing and anticounterfeiting.[1-7] Traditionally, white light generation is realized through the combination of different luminescent centers to reach the appropriate balance of the primary colors red, green and blue (RGB). Alternatively, it can be obtained by the ratiometric fine-tuning of complementary light colours, such as blue and yellow.[1,8-9] Different classes of molecular materials have been so far explored in this field ranging from transition metal[5, 10-11] and lanthanide complexes,[8-9,12-14] to metal-organic extended frameworks,[6-7, 16-17] purely organic polymers[18-19] and discrete molecular units giving rise to excimer (or excimer-like) emission.[20-24] Most often these materials are obtained by incorporating the emissive components into (codoped) polymers, host-guest systems, or by cocrystallization of the selected luminophores. Among the various types of materials, metal-organic luminophores can offer the opportunity to combine light emission of different origins, such as ligand-centered (LC), metal-centered (MC), charge transfer (CT), excimer (EX) or excimer-like (EL), thus significantly expanding the emission range and tunability of the emission colour with respect to fully organic and inorganic materials,[1,5,7] and even adding more functionalities such as magnetic response.[14-15] In particular, lanthanide-based molecular materials are very popular for white light generation and other optical applications in view of the high emission colour purity delivered by the lanthanide intrashell f-f transitions, spanning the entire visible and near-infrared (NIR) spectrum.[8-9] In these systems, the organic ligand typically plays the simultaneous double role of blue light emitter and "antenna" for the indirect sensitization of the lanthanide ions. White light generation is typically obtained by combining the Eu^{3+}/Tb^{3+} red/green emissions with blue light from the organic ligand following a "three component approach",[6,16] whereas dual emissive systems based on the complementary emission colors from Dy^{3+}, Sm^{3+} or Eu^{3+} MC and LC emission are far less explored.[12-15, 17]

However, regardless of the type of compounds used with all these approaches, achieving an accurate balance of the necessary colour components for white light generation in composite systems with multiple emissive centers is a tricky task. While single-phase materials, such as coordination polymers, are indeed sought after to avoid phase separation enabling easier synthetic procedures and processing, synthetic or doping variability, random energy transfer interactions and uncontrolled optical losses involving different optical units statistically distributed in the material may raise problems such as readsorption, poor colour purity and spectral variation.[1,25] This is especially true when the emission originates from different mechanisms from individual emitting centers and is not panchromatic. Integrating the necessary multi-components into a single-phase material allowing for the precise control of the energy transfer phenomena and optical output represents a serious synthetic challenge.[25-27] Hence, because of the

[a] Department of Chemistry, KU Leuven, Celestijnenlaan 200D, 3001, Leuven (Belgium)
[b] Department of Chemical, Mechanical and Materials Engineering, Cagliari State University, via Marengo 2, 09123, Cagliari (Italy).
[c] Department of Chemistry, Ghent University, Krijgslaan 281-S3, 9000, Ghent (Belgium).
[d] Department of Sciences and Technological Innovation, University of Eastern Piedmont "Amedeo Avogadro", Viale Teresa Michel, 11, 15121 Alessandria (Italy)
[e] Hubei Key Laboratory of Ferro & Piezoelectric Materials and Devices, Faculty of Physics & Electronic Sciences, Hubei University, Wuhan 430062 (China)
[f] Department of Civil, Environmental and Architectural Engineering, Cagliari State University, via Marengo 2, 09123, Cagliari (Italy)
† *E-mail: flavia.artizzu@uniupo.it
Electronic Supplementary Information (ESI) available: crystallographic data, powder XRD, thermal analysis data, additional DFT calculations, additional time-resolved PL data, excitation spectra. See DOI: 10.1039/x0xx00000x

DOI: 10.1039/D1TC04015F

intrinsic constraints, it is not surprising that single-phase pure white light emitters based on small molecules still remain rare. In this work, we present a quite unique example of a single-component panchromatic white light emitter based on a Dy quinolinolate complex which also displays NIR luminescence. Quinolinolate metal complexes have been widely explored for their use as emissive centres in OLED devices thanks to the semiconducting properties of the ligand, their thermal stability and remarkable optical performances.[28-32] In the presented complex, extensive π-stacking interactions between quinoline units in the crystalline state induce broad ligand-related spectral emission covering almost the entire visible range with relatively high quantum yield. The aggregation-induced origin of this emission allows for luminescence color tuning from green to orange upon dissolution in organic solvent and mechanical stimuli. In addition, the compound displays strong Dy-centered NIR luminescence upon excitation in an extraordinarily broad spectral range. The origin of the observed optical features were investigated by absorption and photoluminescence measurements with the support of Density Functional Theory calculations.

Results and Discussion

Synthesis, crystal structure description and thermal analysis

$Dy(ClQ)_2(HClQ)_2Cl]$ (HClQ = 5,7-dichloro-8-quinolinol) (**1**) was synthesized by reacting dysprosium chloride and the HClQ ligand in appropriate ratio under neutral conditions in a CH_3CN/CH_3OH solvent mixture according to the procedure described in the Experimental section.[31] Slow solvent evaporation of the supersaturated solution afforded well-formed prismatic red crystals. X-ray diffraction (XRD) structural investigation (Figure 1) reveals that the molecular unit of **1** consists of four quinolinol ligand derivatives and one chloride ion coordinated to Dy^{3+}. Out of the four coordinated ligands, two are bidentate anions and two are in the neutral form as zwitterions (NH^+,O^-), acting as monodentate donors (Figure 1a). Intramolecular hydrogen bonding interactions are established between the protons on the N donor atoms and the O atoms of opposite ligand units. The Dy^{3+} ion is therefore heptacoordinated by four oxygen, two nitrogen donor atoms and a chloride and adopts a distorted pentagonal bipyramidal geometry (Figure 1b). The compound crystallizes in the non-centrosymmetric $Pca2_1$ space group where single molecules organize into dimeric units related by a pseudo-center of symmetry (Figure 1c). An extensive network of π-stacking interactions both intra- and inter-dimers is established in the crystal packing (Figures 1c,d,e). Crystallographic data are reported in Table 1. Powder XRD (PXRD) measurements confirm the phase purity of the sample (Figure S1).
Thermal analysis, shown in Figure S2, reveal that the compound is thermally stable, with no relevant weight losses, up to temperatures above 250°C.

Optical absorption and structure-properties relationship

The diffuse absorbance (DA) spectrum of **1** in the crystalline state is reported in Figure 2. Several Dy^{3+} -centered peaks related to f-f transitions from the ground state $^6H_{15/2}$ to superior energy levels are recognizable in the NIR region. A very broad absorption band, which can be roughly associated to ligand-related π-π* transitions, dominates the UV-visible region with a cutoff at ~585 nm. A close inspection of the band shape and the comparison with the spectral profile of **1** in CH_3OH solution (see inset in Figure 2) evidences the appearance of an additional shoulder related to a low energy absorption. Spectral deconvolution confirms the contribution of two bands centered at 343 and 409 nm, very similar to the spectral features observed in solution (λ_{max} = 335 and 399 nm), and an additional band peaked at 508 nm. This latter feature accounts for the intense red color of the crystals in contrast to the yellow color of the diluted solution, clearly indicating that solid-state interactions allow for new electron transitions in the molecular assembly.

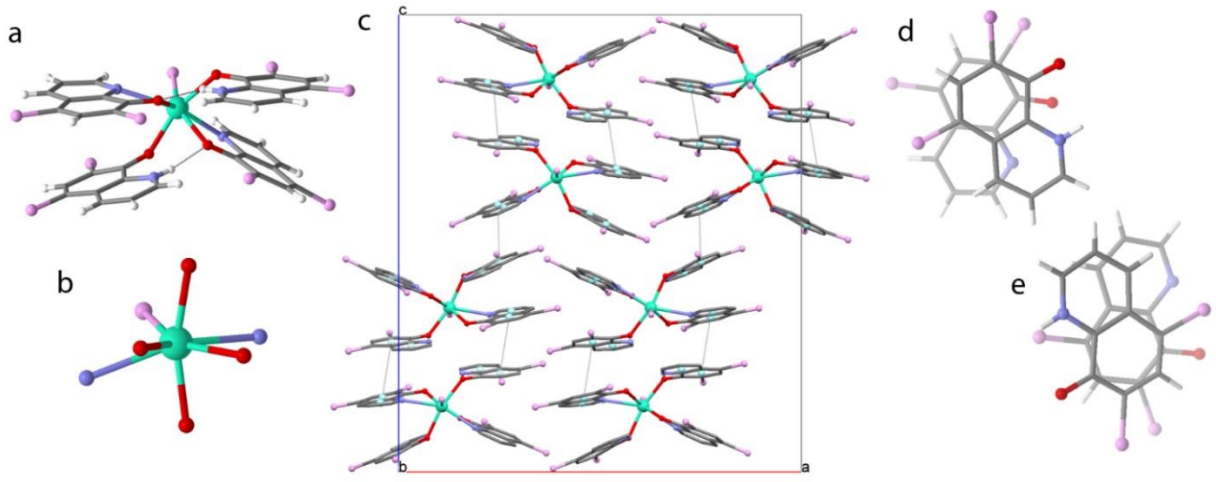

Figure 1. Crystal structure of **1**. a) molecular unit; b) Dy^{3+} coordination environment; c) crystal packing viewed down the *b* crystallographic axis; d) intra-dimer stack of ligand units; e) inter-dimer stack of ligand units. Intramolecular hydrogen bonds (a) and intermolecular π-π stacking interactions (<3.6 Å) between ring centroids (light blue spheres) of adjacent ligand units (c) are evidenced by dashed grey lines. Color codes: green, Dy; red, O; blue, N; purple, Cl; grey C; white, H.

View Article Online
DOI: 10.1039/D1TC04191F

ARTICLE

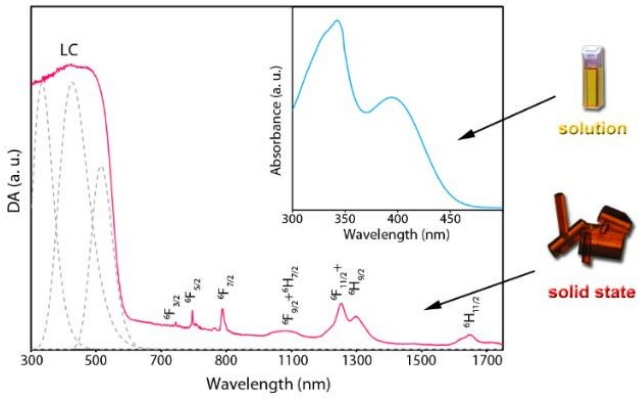

Figure 2. DA spectrum of **1** in the crystalline state (red solid line) and deconvoluted bands of ligand-related absorption (grey dashed lines). The spectroscopic terms related to the Dy^{3+}-centered transitions from the $^6H_{15/2}$ ground state are indicated. Inset reports the absorption profile of **1** in CH_3OH solution (blue solid line). Spectral deconvolution was carried out on the energy scale and herein reported in wavelength.

To better clarify the origin of the optical features in the crystalline state, we performed density functional theory (DFT) calculations to investigate the electronic structure of the compound. In order to reduce highly expensive computational costs, **1** was modelled by replacing the trivalent $4f^9$ Dy^{3+} ion with the $4f^0$ Y^{3+} ion (**1'**) This choice was made by reasonably assuming that the above described optical properties in the visible are solely originated from ligand states and that the lanthanide ion does not significantly contribute to the frontier molecular orbitals (MOs). This approach has been already demonstrated successful in describing the optical features of lanthanide complexes.[34-35] In particular, herein the main interest is to unravel the role of intermolecular interactions between adjacent ligands on the optical properties of **1**. To this purpose, DFT calculations were performed by taking into consideration three different configurations in the crystal packing, as schematized in Figure S3 in Supporting Information. These consist of a single molecule ("monomer"), a dimeric unit ("dimer") and a set of three molecules that are part of three different dimeric units ("inter-dimer" configuration). Figure 3a shows the calculated frontier molecular orbitals (MOs) for **1'** in the "inter-dimer" configuration which reveal that the electron density is highly localized on (H)ClQ ligands with no metal contribution for the first highest occupied MOs (HOMOs) and the first lowest unoccupied MOs (LUMOs), similarly to the "monomer" and "dimer" configurations (Figures S4-S6). MOs energy splitting following supramolecular combinations results in the generation of a band-like configuration.

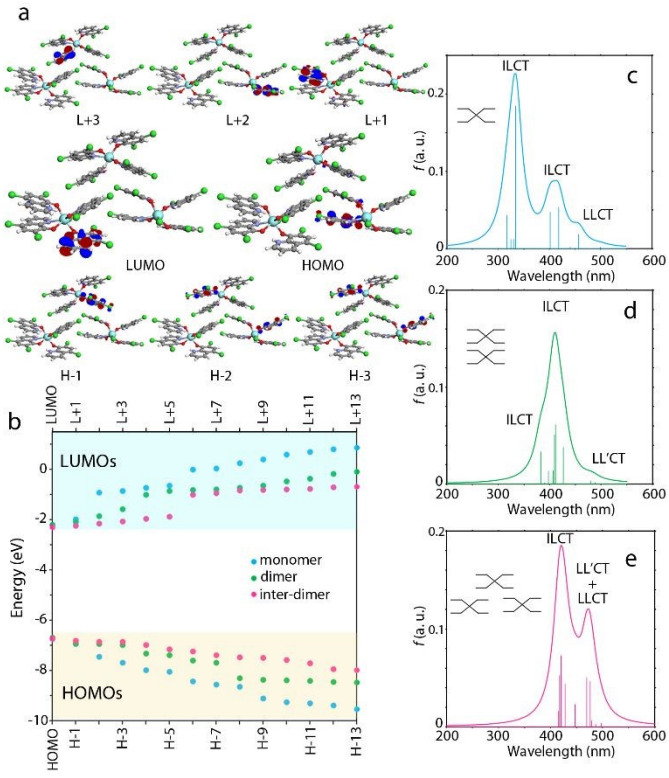

Figure 3. a) DFT-calculated frontier MOs of **1'** in the crystalline state as "inter-dimer" configuration. b) energies of the first sets of HOMOs and LUMOs and c, d, e) TD-DFT calculated absorption spectra for **1'** as "monomer", "dimer" and "inter-dimer" configurations, as illustrated in the insets.

The DFT-calculated energy sequence of the frontier MOs (Figure 3b) evidences the narrowing of the band gap between the last set of HOMOs and the first set of LUMOs which become more closely spaced on extending the intermolecular interactions from the monomer to the "inter-dimer" arrangement. This result is consistent with the absorption spectra retrieved from time-dependent TD-DFT calculations (first 10 states) shown in Figures 3c, d and e for the three types of the above mentioned configurations as depicted in the insets. The spectrum of Figure 3e is dominated by two main peaks that closely resemble those retrieved from the spectral deconvolution of the DA of **1** in the crystalline state (Figure 2). Instead, the spectral profile calculated for the monomer configuration (Figure 3c) is almost superimposable to that observed for **1** in CH_3OH solution, as expected. These results suggest that the origin of the low-energy absorption band in the crystalline state is mainly related to interactions between adjacent ligand moieties of different discrete dimers. This may not be surprising when considering that the "inter-dimer" overlap of quinoline rings is more effective than intra-dimer (Figure 1e). The analysis of TD-DFT

data (Table S2) shows that, whereas higher energy transitions are mainly of intra-ligand charge transfer (ILCT) character, on lowering the energy they become predominantly ligand-to-ligand charge transfer, either intra- (LLCT) and inter-molecular (LL'CT), evidencing the role of π-stacking interactions in the low energy absorption features.

Photoluminescence

White light emission and mechanochromic behavior Photoluminescence (PL) steady-state measurements shown in Figure 4a on **1** as bulk crystals reveal a very broad emission profile covering almost the entire visible spectral range up to ~680nm upon excitation in the UV region. Two distinct emission bands are clearly recognizable, one peaked at 480 nm, falling in the blue-green spectral region, and one centered at 620 nm corresponding to an orange-red light component. As a result, the combination of these two emissions gives rise to pure white light with CIE (Commission Internationale de l'Éclairage) coordinates x, y 0.33, 0.33 (Figures 4b,c) and a PL quantum yield (PLQY) of ~14% which is relatively high among those reported for molecular white-light emitting materials.[5,8] The characteristics of the observed spectral profile are consistent with those typical of a π-stacked aromatic organic system displaying excimer-like (EL) emission.[24, 36-37] Short-contact (<0.4 nm) interactions favor supramolecular energy states that give rise to intermolecular CT transitions at significant lower energy than single-molecule transitions.[20] As a result, intense emission in the orange-red spectral-range is observed for **1** in the crystalline state, in sharp contrast with the green monomer emission observed in diluted solution (Figures 4a,b). It must be mentioned that the term "excimer-like" is more appropriately used here in place of "excimer" as the observed behavior is ascribed to a preformed molecular arrangement in the crystalline state, not a photoinduced one.[37] The emission contribution in the blue-green region is instead of less obvious attribution but the similarity to the monomer emission in solution and the ILCT character of the high energy transitions may indicate that it originates from locally excited (LE) "monomer" states.[§] This attribution is also supported by time-resolved measurements (Figure 4d) which evidence the significantly longer decay dynamics (τ_{av} = 5.5 ns)[§§] of the EL decay at 620 nm with respect to the emission at 480 nm, displaying a sub-ns decay.[36] This observation is also confirmed by the measurements made on the isostructural gadolinium analog,[33] where no ligand to metal energy transfer can occur (*vide infra*), which displays an outstandingly long lived decay of hundreds of ns for the emission at 620 nm (Figure S7 and related discussion in SI). Interestingly, upon gentle sample grinding, the high energy emission band completely disappears whereas the lower energy one is enhanced (Figure 4a) and the sample luminescence color turns from white to orange-red (Figures 4b,c). This phenomenon confirms the EL nature of the emission which is typically sensitive to mechanical stress.[23] In this case, since no obvious change in the PXRD pattern is observed (Figure S1), we can argue that grinding leads to a compression of the supramolecular structure with an enhancement of the short contact π interactions. It is interesting to note that the excitation spectrum of the EL emission at 620 nm covers the entire absorption range (Figure S7), implying high color stability. To the best of our knowledge, this is the first example of rare orange-red[35] excimer-like emission in a quinoline derivative.

NIR emission Remarkably, **1** additionally displays intense Dy-centered NIR PL (Figure 4e) upon excitation in the whole ligand absorption range (Figure S8) at 990 and 1325 nm. This latter line falls in the O-band of the optical fibers telecommunication range and is seldom observed in Dy^{3+} complexes. On the other hand, no characteristic emission peak of Dy^{3+} is recognizable in the visible likely due to the energy mismatch between the excited levels of the quinoline ligand derivative and the emitting $^4F_{9/2}$ level of Dy^{3+} at ~21000 cm^{-1} (Figure 4f). For this reason, the two intense NIR bands were assigned to transitions from low energy states of Dy^{3+} ($^6H_{5/2}$ + $^6F_{9/2}$ and $^6H_{9/2}$ for the emission at 990 nm and at 1325 nm, respectively) to the ground $^6H_{15/2}$ state.[38-39] The excitation spectrum of the NIR transitions in Figure S7 indicates that both high energy ILCT and lower energy LLCT+LL'CT states of the ligand can populate the Dy^{3+} ^6H_J levels. This combined contribution allows for optical pumping of NIR emission across an extraordinarily broad spectral range. The sensitization mechanism is believed to occur through the activation of intermediate ligand triplet states triggered by the presence of the lanthanide ion (Figure 4f), thus accounting for the relatively shortened lifetimes of LC fluorescence with respect to analogous p-metal derivatives (>8 ns).[40] The Dy^{3+} sensitization efficiency can be estimated through the comparison of the decay dynamics of the ligand energy donor states in the reference isostructural derivative of the optically silent Gd^{3+}, which cannot act as acceptor due to the very high energy of its level manifolds (Figure S7). Significantly longer decay time constants with respect to those observed for **1** (Figure 4d) were retrieved for both the LLCT/LL'CT states, giving rise to the EL emission (τ_{Gd} = 307 ns vs τ_{Dy} = 5.5 ns), and the ILCT states related to the LE component (τ_{Gd} = 1.57 ns vs τ_{Dy} < 1 ns, resolution limited), confirming that the Dy^{3+} NIR-emitting energy levels can be efficiently excited over the whole visible absorption range. These data yield an estimation of the Dy^{3+} sensitization efficiency of over 98% (calculation details are reported in Supporting Information). Time constants of τ = 16.0 μs and 8.2 μs are retrieved by monoexponential curve fitting of the decay at 990 nm and 1325 nm, respectively (Figure 4g). Taking an estimation of the Dy^{3+} radiative lifetime τ_{rad} (defined as the lifetime of the emitter in the absence of external quenchers) in a molecular complex of 243 and 394 μs for the emission from the $^6H_{5/2}$ and $^6H_{9/2}$ levels, respectively,[38] the Dy^{3+} intrinsic quantum yield can be calculated through the equation $\Phi_{Dy} = \tau/\tau_{rad}$, yielding values of Φ_{990} = 6.6% and Φ_{1325} = 2.1%.
The above discussed figures of merit may make **1** more promising for optical amplification in the NIR over the traditionally used Er complexes (emitting in the optical C-band),[29-30] thus opening new perspectives for the exploitation of the telecom O-band.

View Article Online
DOI: 10.1039/D1TC04191F

ARTICLE

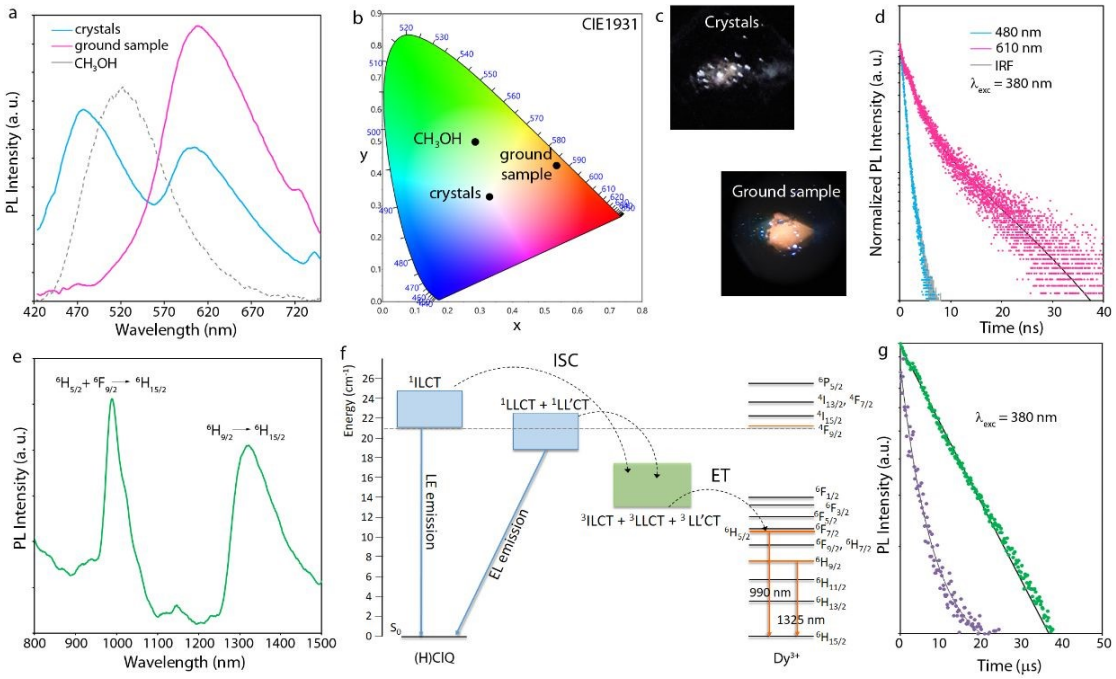

Figure 4. a) PL spectra of **1** as bulk crystals, ground sample and in CH_3OH solution excited at 380 nm; b) CIE 1931 chromaticity diagram for **1** emission in bulk crystals (x, y 0.33, 0.33), as ground sample (x, y 0.54, 0.43) and in CH_3OH solution (0.29, 0.50); c) photographs of **1** as bulk crystals (above) and ground sample (below) under UV light illumination (380 nm); d) Time-resolved decay curves in the visible range; e) NIR emission spectrum upon excitation at 380 nm; f) Jablonski diagram illustrating the energy flow pathways in **1**. Solid arrows represent radiative emission, dashed arrows represent non-radiative decay channels; g) decay dynamics of Dy-centred emission at 990 nm ($^6H_{5/2}$, green dots) and at 1325 nm ($^6H_{9/2}$, purple dots).

Conclusions

In conclusion, the presented $[Dy(ClQ)_2(HClQ)_2Cl]$ complex is a rare case of single-component single-molecule white light emitter in the solid state which also displays mechanochromic luminescence and remarkable NIR emission at telecommunication wavelengths. Here, the lanthanide ion not only acts as an active emitting centre, but also templates the molecular structural arrangement giving rise to an extensive π-stacking of quinolinol moieties between discrete dimeric units in the crystal packing. As a result, a peculiar ligand-centred excimer-like luminescence in the orange-red spectral region is observed which significantly deviates from the green monomer emission in solution and combines to locally excited blue-green luminescence in crystals to yield pure white light. Furthermore, both monomer and excimer-like states can sensitize Dy-centered NIR emission allowing for optical pumping in an extraordinarily broad spectral range. These features, along with the known semiconducting properties of such quinoline complex derivatives, make this compound promising for a number of applications in OLEDs, telecommunication, sensing or security applications.

Experimental

Synthesis

Chemicals: All reagents and solvents were purchased from Aldrich and used without further purification.

*Synthesis of [Dy(5,7ClQ)$_2$(H5,7ClQ)$_2$Cl] (**1**):* The synthesis was carried out following a previously optimized procedure.[31] A solution of 0.5 mmol (188.5 mg) of $DyCl_3 \cdot 6H_2O$ dissolved in 10 mL of of CH_3CN/CH_3OH (4:1 v/v) was slowly added to a solution of 2 mmol (428.3 mg) of HClQ in the same solvent mixture. After 24 hours of stirring at 50-60°C the yellow solution was roto-evaporated until it turned orange and was left standing to the air. After a few days block red crystals, suitable for X-ray studies, were collected and washed with diethyl ether (yield 49%). CHN: Found (Calcd for $C_{36}H_{18}Cl_9DyN_4O_4$) C% 41.05(41.10), H% 1.63(1.72), N% 5.37(5.33). FT-IR (KBr pellet, cm^{-1}): 3236 vw, 3171 vw, 3102 w, 3026 w, 2966 w, 2914 w, 2850 vw, 2752 vw, 2116 w(ν N^+–H), 2013 w, 1616 m, 1592 w, 1560 s, 1544 m, 1489

m, 1455 vs, 1394 m, 1364 s, 1314 m, 1292 w, 1250 w, 1232 mw, 1220 m, 1194 m, 1144 m, 1106 m (split peak), 1051 mw (δ C–H), 991 vw, 957 m (ν C–Cl), 876 m (ν C–Cl), 810 m, 789 m, 749 s (split peak), 672 m, 659 m, 646 w, 634 m, 585 w, 571 mw, 505 m, 422 mw. *Synthesis of [Gd(5,7ClQ)$_2$(H5,7ClQ)$_2$Cl]:* The synthesis was carried out with a similar procedure as **1**, using the appropriate $GdCl_3 \cdot 6H_2O$ salt and the compound was characterized as previously described.[33]

Characterization.

Electronic UV-Vis-NIR spectroscopy. Diffuse absorbance (DA) spectra on solid state samples were acquired in the 200–2000 nm range with a Varian Cary 5 spectrometer equipped with a 150 mm diameter integrating sphere on samples dispersed on Teflon film. Absorption spectra of solution samples were acquired in the 350–2000 nm range with a PerkinElmer Lambda 950 spectrometer, in a quartz cuvette of 10 mm path length (Starna cuvette type 23/Q/10).

Vibrational spectroscopy. Fourier Transform Infrared (FTIR) spectra of samples dispersed on KBr pellets were acquired in the region of 400–4000 cm^{-1}with a Thermo Scientific Nicolet 6700 FT-IR spectrometer equipped with a nitrogen-cooled Mercury Cadmium Telluride (MCT) detector and KBr beam splitter.

Elemental analysis. Elemental analysis (C, H, N) was performed on a Thermo Flash 2000 elemental analyzer. V_2O_5 was used as catalyst.

Thermal analysis. Thermal gravimetric analysis (TG) and simultaneous differential thermal analysis (DTA) were carried out on a Mettler-Toledo TGA/STDA 851. Thermal analysis data were collected in the 25–800 °C range, under oxygen flow (heating rate = 10 °C min−1; flow rate = 50 mL min^{-1}).

Single-crystal X-ray diffraction. X-ray data collection was performed at 100 K on a Rigaku Oxford Diffraction Supernova Dual Source diffractometer equipped with an Atlas CCD detector using ω scans Cu Kα (λ= 1.54184 Å) radiation. The images were interpreted and integrated with the program CrysAlisPro (Rigaku Oxford Diffraction)[41] using Olex2.[42] The structure was solved by direct methods using the ShelXS structure solution program and refined by full-matrix least-squares on F^2 with full-matrix least squares using the ShelXL program package.[43-44] Non-hydrogen atoms were anisotropically refined. CCDC 1990016 contains the supplementary crystallographic data for this paper. These data can be obtained free of charge from The Cambridge Crystallographic Data Centre via www.ccdc.cam.ac.uk/structures.

Powder X-ray diffraction. Wide-angle X-ray diffraction XRD patterns were recorded on a Thermo Scientific ARL X ' TRA diffractometer. The scans were collected at a scan rate of 1° min^{-1} within the range 5–40° (2θ) using Cu Kα radiation.

Photoluminescence measurements.

Photoluminescence (PL) measurements were performed using an Edinburgh FLSP920 spectrophotometer equipped with a Hamamatsu R928P PMT detector (200–900 nm) and a Hamamatsu R5509-72 NIR PMT detector (500–1700 nm). Steady-state PL spectra were acquired using a 450W continuous-wave (CW) xenon lamp, whereas a pulsed Xe lamp (repetition rate 100 Hz; 60 W) and a Fianium Supercontinuum white light laser (repetition rate 20 MHz, pulse width 80 ps) were used for time-resolved measurements. Appropriate optical filters were used, and steady-state emission data were corrected for the spectral response. All luminescence measurements were recorded at room temperature. Crystals were put between quartz plates (Starna cuvettes type 20/C/Q/0.2). The internal quantum yield was measured using an integrating sphere (110 mm diameter) on the FLSP920 spectrophotometer, and white $BaSO_4$ powder was used as a reference to measure the scattered excitation light. The internal quantum yield Φ was calculated through the following equation:

$$\Phi = \frac{\varepsilon}{\alpha} = \frac{\int L_s}{\int E_R - \int E_s} \qquad \textbf{Equation 1}$$

where ε is the number of photons emitted by the sample and α is the number of photons absorbed by the sample. L_S is the luminescence emission spectrum of the sample; E_R is the spectrum of the scattered excitation light with the $BaSO_4$ reference sample in the sphere; E_S is the spectrum of the scattered excitation light with the actual sample in the sphere. Additional time-resolved measurements on [Gd(5,7ClQ)$_2$(H5,7ClQ)$_2$Cl] crystals were acquired with a Horiba Scientific Fluorolog spectrofluorimeter using a time-correlated single-photon-counting technique, with a pulsed excitation source, NanoLed, at 370 nm (Horiba) at an impulse repetition rate of 1 MHz at 90° geometry to the R928 detector (Hamamatsu).

DFT Calculations.

Electronic structure calculations were performed at Density Functional Theory (DFT)[45] level employing the GAUSSIAN 16[46] software package. The functionals used throughout this study was CAM-B3LYP;[47] basis set 6-31+G(d,p)[48] was used for atoms C, H, O, N S, Cl and LANL2DZ ECP basis set[49] on Y. All calculations were input using atomic coordinates obtained from single X-ray data. The 10 lowest singlet excited states of the closed shell were calculated within the time-dependent DFT (TDDFT) calculations using the formalism as implemented in GAUSSIAN 16.[46] The orbital isosurfaces were visualized using ArgusLab 4.0[50] whereas the calculated UV-Vis electronic spectra were visualized with Gabedit 2.5.0[51] software.

Conflicts of interest

There are no conflicts to declare.

Acknowledgements

DM acknowledges KU Leuven Postdoctoral Mandate Internal Funds (PDM) for a postdoctoral fellowship (PDM/20/092). KVH thanks the Research Foundation – Flanders (FWO) (projects AUGE/11/029 and G099319N) for funding.

Notes and references

§ It should be nonetheless noted that self absorption phenomena can occur in the blue-green spectral region which can contribute to a significant distortion of the spectrum.
§§ The decay curve is best fitted with a biexponential function, likely reflecting local differences of emitting sites in the bulk crystalline material. This observation is also consistent with the dependence of the emission on the crystal packing. However, a small fast component related to the partially overlapping LE emission cannot be excluded.

1 M. Pan, W. M. Liao, S. Y. Yin, S. S. Sun and C. Y. Su *Chem. Rev.* 2018, **118**, 8889.
2 Q. Wang and D. Ma *Chem. Soc. Rev.* 2010, **39**, 2387.
3 H. B. Wu, L. Ying, W. Yang and Y. Cao *Chem. Soc. Rev.* 2009, **38**, 3391.
4 K. T. Kamtekar, A. P. Monkman and M. R. Bryce *Adv. Mater.* 2010, **22**, 572.
5 J. Miao, Y. Nie, Y. Li, C. Qin, Y. Ren, C. Xu, M. Yan, K. Liu and G. Liu *J. Mater. Chem. C* 2019, **7**, 13454.
6 Z. Zhang, N. Ma, S. Yao, W. Han, X. Li, H. Chang and Y.-Y. Wang *ACS Sust. Chem. Eng.* 2021, **9**, 17, 5827.
7 B.-B. Du, Y.-X. Zhu, M. Pan, M.-Q. Yue, Y.-J. Hou, K. Wu, L.-Y. Zhang, L. Chen, S.-Y. Yin, Y.-N. Fan and C.-Y. Su *Chem. Commun.* 2015, **51**, 12533.
8 S. SeethaLekshmi, A.R. Ramya, M.L.P. Reddy and S. Varughese *J. Photochem. Photobio. C: Photochemistry Reviews* 2017, **33**, 109.
9 P. Li and H. Li *Coord. Chem. Rev.*, 2021, **441**, 213988.
10 M. S. Wang, S. P. Guo, Y. Li, L. Z. Cai, J. P. Zou, G. Xu, W. W. Zhou, F. K. Zheng and G. C. Gou *J. Am. Chem. Soc.* 2009, **131**, 13572.
11 Z. Chen, D. Wu, X. Han, J. H. Jiang, J. Yin, G. A. Yu and S. H. Liu *Chem. Commun.* 2014, **50**, 11033.
12 Q.-Y. Yang, K. Wu, J.-J. Jiang, C.-W. Hsu, M. Pan, J.-M. Lehn and C.-Y. Su *Chem. Commun,* 2014, **50**, 7702.
13 Y.-Yi. Xu, P. Chen, T. Gao, H.-F. Li and P.-F. Yan *Cryst. Eng. Comm.* 2019, **21**, 964.
14 L. Zhing, W.-B. Chen, Z.-J. OuYang, M. Yang, Y.-Q. Zhang, S. Gao, M. Schulze, W. Wernsdofer and W. Dong *Chem. Commun.* 2020, **56**, 2590.
15 J. Wang, S. Chorazy, K. Nakabayashi, B. Sieklucka and S. Ohkoshi *J. Mater. Chem. C* 2018, **6**, 473.
16 Zhang, Y. Chen, H. Chang, Y. Wang, X. Li and X. Zhu *J. Mater. Chem. C* 2020, **8**, 2205.
17 C. Yang, F. Artizzu, K. Folens, G. Du Laing and R. Van Deun *J. Mater. Chem. C* 2021, **9**, 7154.
18 J. Luo, X. Li, Q. Hou, J. B. Peng, W. Yang and Y. Cao *Adv. Mater.* 2007, **19**, 1113.
19 A. J. Sandee, C. K. Williams, N. R. Evans, J. E. Davies, C. E. Boothby, A. Kohler, R. H. Friend and A. B. Holmes, *J. Am. Chem. Soc.* 2004, **126**, 7041.
20 Q.-Y. Yang and J.-M. Lehn *Angew. Chem. Int. Ed.* 2014, **53**, 4572.
21 Y.-H. Chen, K.-C. Tang, Y.-T. Chen, J.-Y. ShenY.-S. Wu, S.-H. Liu, C.-S. Lee, C.-H. Chen, T.-Y. Lai, S.-H. Tung, R.-J. Jeng, W.-Y. Hung, M. Jiao, C.-C. Wu and P.-T. Chou *Chem. Sci.* 2016, **7**, 3556.
22 Y. Liu, H. Liu, Q. Bai, C. Du, A. Shang, D. Jiang, X. Tang and P. Lu *ACS Appl. Mater. Interfaces* 2020, **12**, 16715.
23 L.Y. Hsu, S. Maity, Y. Matsunaga, Y.-F. Hsu, Y.-H. Liu, S.-M. Peng, T. Shinmyozu and J.-S. Yang *Chem. Sci.* 2018, **9**, 8990.
24 V. Kumar, B. Sk, S. Kundu and A. Patra ***J. Mater. Chem. C*** 2018, **6**, 12086.
25 Y. Pointel, F. Houard, Y. Suffren, C. Daiguebonne, F. Le Natur, S. Freslon, G. Calvez, K. Bernot and O. Guillou *Inorg. Chem.* 2020, **59**, 15, 11028.
26 F. Artizzu, F. Quochi, A. Serpe, E. Sessini and P. Deplano *Inorg. Chem. Front.* 2015, **2**, 213.
27 F. Artizzu, F. Quochi, L. Marchiò, R. Fonseca Correia, M. Saba, A. Serpe, A. Mura, M. L. Mercuri, G. Bongiovanni and P. Deplano *Chem. A Eur. J.* 2015, **21**, 3882.
28 C.W. Tang and S. A. Van Slyke *App. Phys. Lett.* 1987, **51**, 913.
29 R. J. Curry and W. P. Gillin *Appl. Phys. Lett.* 1999, **75**, 1380.
30 L. Wang, Z. Zhao, C. Wei, H. Wei, Z. Liu, Z. Bian and C. Huang *Adv. Optical Mater.* 2019, 1801256.
31 F. Artizzu, P. Deplano, L. Marchiò, M. L. Mercuri, L. Pilia, A. Serpe, F. Quochi, R. Orrù, F. Cordella, M. Saba, A. Mura and G. Bongiovanni *Adv. Funct. Mater.* 2007, **17**, 2365.
32 R. Van Deun, P. Fias, P. Nockemann, A. Schepers, T. N. Parac-Vogt, K. Van Hecke, L. Van Meervelt and K. Binnemans *Inorg. Chem.* 2004, **43**, 8461.
33 F. Artizzu, K. Bernot, A. Caneschi, E. Coronado, J. M. Clemente-Juan, L. Marchiò, M. L. Mercuri, L. Pilia, A. Serpe and P. Deplano, *Eur. J. Inorg. Chem.* 2008, 3820.
34 F. Gutierrez, C. Tedeschi, L. Maron, J.-P. Daudey, J. Azema, P. Tisnès, C. Picard and R. Poteau J. Mol. Struct.: THEOCHEM 2005, **756**, 151.
35 E. G. Moore, J. Xu, C. J. Jocher, I. Castro-Rodriguez and Kenneth N. Raymond *Inorg. Chem.* 2008, **47**, 3105.
36 Y. Shen, Z. Zhang, H. Liu, Y. Yan, S. Zhang, B. Yang and Y. Ma *J. Phys. Chem. C* 2019, **123**, 13047.
37 N. K. Al-Rasbi, C. Sabatini, F. Barigelletti and M. D. Ward *Dalton Trans.* 2006, 4769.
38 N. Kofod, R. Arppe-Tabbara and T. Sørensen *Phys. Chem. A* 2019, **123**, 13, 2734.
39 W. T. Carnall, G. L. Goodman, K. Rajnak and R. S. Rana *J. Chem. Phys.* 1989, **90**, 7, 3443.
40 F. Quochi, M. Saba, F. Artizzu, M. L. Mercuri, P. Deplano, A. Mura and G. Bongiovanni *J. Phys. Chem. Lett.* 2010, **1**, 2733.
41 Rigaku Oxford Diffraction. CrysAlis Pro Rigaku Oxford Softwar System, Rigaku Corporation, UK, 2015.
42 O. V. Dolomanov, L. J. Bourhis, R. J. Gildea and J. A. K. Howard and H. Puschmann *J. Appl. Cryst.* 2009, **42**, 339.
43 G. M. Sheldrick *Acta Cryst. Sect. A* 2008, **64**, 112.
44 G. M. Sheldrick *Acta Cryst. Sect. C* 2015, **71**, 3.
45 R. G. Parr, W. Yang Density Functional Theory of Atoms and Molecules; Oxford University Press: Oxford, 1989.
46 Gaussian 16, Revision C.01, M. J. Frisch, G. W. Trucks, H. B. Schlegel, G. E. Scuseria, M. A. Robb, J. R. Cheeseman, G. Scalmani, V. Barone, G. A. Petersson, H. Nakatsuji, X. Li, M. Caricato, A. V. Marenich, J. Bloino, B. G. Janesko, R. Gomperts, B. Mennucci, H. P. Hratchian, J. V. Ortiz, A. F. Izmaylov, J. L. Sonnenberg, D. Williams-Young, F. Ding, F. Lipparini, F. Egidi, J. Goings, B. Peng, A. Petrone, T. Henderson, D. Ranasinghe, V. G. Zakrzewski, J. Gao, N. Rega, G. Zheng, W. Liang, M. Hada, M. Ehara, K. Toyota, R. Fukuda, J. Hasegawa, M. Ishida, T. Nakajima, Y. Honda, O. Kitao, H. Nakai, T. Vreven, K. Throssell, J. A. Montgomery, Jr., J. E. Peralta, F. Ogliaro, M. J. Bearpark, J. J. Heyd, E. N. Brothers, K. N. Kudin, V. N. Staroverov, T. A. Keith, R. Kobayashi, J. Normand, K. Raghavachari, A. P. Rendell, J. C. Burant, S. S. Iyengar, J. Tomasi, M. Cossi, J. M. Millam, M. Klene, C. Adamo, R. Cammi, J. W. Ochterski, R. L. Martin, K. Morokuma, O. Farkas, J. B. Foresman, and D. J. Fox, Gaussian, Inc., Wallingford CT, 2016.
47 T. Yanai, D. Tew, and N. Handy, *Chem. Phys. Lett*., 2004, **393**, 51.
48 G. A. Petersson, A. Bennett, T. G. Tensfeldt, M. A. Al-Laham, W. A. Shirley, and J. Mantzaris, *J. Chem. Phys*., 1988, **89**, 2193.
49 P.J. Hay, W.R. Wadt, *J. Chem. Phys*., 1985, **82**, 299.
50 Thompson, M. A. ArgusLab 4.0.1; Planaria Software LLC: Seattle, WA, http://www.arguslab.com/arguslab.com/ArgusLab.html/.

51 A.R. Allouche, *J. Comput. Chem.*, 2011, **32**, 174.

View Article Online
DOI: 10.1039/D1TC04191F